ORIGINAL RESEARCH ARTICLE

Understanding the Effects of $CoAl_2O_4$ Inoculant Additions on Microstructure in Additively Manufactured Inconel 718 Processed *Via* Selective Laser Melting

DHRUV TIPARTI, I-TING HO, KAI-CHUN CHANG, TZU-HOU HSU, AN-CHOU YEH, and SAMMY TIN

The effect of varying amounts of $CoAl_2O_4$ inoculant ranging from 0 to 2 wt pct on the microstructure evolution of Inconel 718(IN718) fabricated by selective laser melting (SLM) was evaluated. Characterization of the as-built microstructure revealed that addition of $CoAl_2O_4$ resulted in a modest degree of grain refinement with a slight increase in microstructural anisotropy. Increasing the total $CoAl_2O_4$ content beyond 0.2 wt pct resulted in severe agglomeration of the non-metallic particles and the formation of slag inclusions measuring up to 100 μm in size present in the as-built microstructure. In addition to large agglomerates, the inoculant was chemically reduced to form a fine dispersion of submicron-sized Al_2O_3 particles throughout the IN718 matrix. The fine dispersion of oxides significantly hindered grain recrystallization during the post-fabrication heat treatment due to a Zener pinning effect. The findings from this study indicate in order to effectively utilize $CoAl_2O_4$ as a grain refining inoculant for additive manufacturing, the process parameters need to be optimized to avoid agglomeration of the non-metallic particles and other process-related defects.

https://doi.org/10.1007/s11661-021-06255-z

I. INTRODUCTION

PROGRESS in fusion-based additive manufacturing (AM) has led to the ability of producing complex near-net shape components that are difficult to produce by conventional manufacturing methods such as casting, forging, and/or machining.[1] The AM of Ni-based superalloys is of particular interest due to the outstanding high-temperature mechanical properties and degradation resistance enabled by a number of complex alloying additions. Ni-based superalloys are widely used in aerospace and power-generation industries, with the primary application towards gas turbine engines where they constitute ~ 40 to 50 pct of the total weight.[2] For these applications, AM is particularly advantageous for transforming traditional design methodologies that reduce the number of assembly components or integrate advanced cooling configurations. The above cases can lead to significant economic and performance-related benefits. However, with most components being of structural importance, the application of laser bed powder fusion AM parts is limited due to the process leading to an intrinsically anisotropic microstructure consisting of highly textured columnar grains. This resulting mechanical anisotropy is one of the limiting factors inhibiting the widespread adoption and applicability of AM-processed Ni-superalloys in gas turbine engines.[1,3–5]

The microstructural anisotropy arises from the requirement to produce fully dense parts during the AM process, which in turn requires partial remelting of the underlying layer or substrate.[1,6–8] Under these conditions, the barrier for nucleation to occur, in terms of nucleation undercooling (ΔT_n), is effectively zero, leading to the epitaxial growth of the underlying grains. Growth of these grains tends to occur in the maximum thermal gradient direction (G) or direction normal to the deposited layer. As discrete layers are gradually accumulated to create a 3D shape, the iterative melting and epitaxial solidification cycles lead to the formation of a textured, columnar microstructure due to the competitive growth of grains.[9–11] However, growth of equiaxed grains may still occur ahead of the columnar grains, which provided there is enough constitutional

DHRUV TIPARTI, I-TING HO, and SAMMY TIN are with the Department of Mechanical, Materials and Aerospace Engineering, Illinois Institute of Technology, Chicago, IL 60616. Contact e-mail: dtiparti@hawk.iit.edu KAI-CHUN CHANG, TZU-HOU HSU, and AN-CHOU YEH are with the Department of Materials Science and Engineering, National Tsing Hua University, Hsinchu, 30013, Taiwan (R.O.C.).

Manuscript submitted December 18, 2020, accepted March 18, 2021.

Article published online April 5, 2021

supercooling (ΔT_C) corresponding to the ΔT_n required for nucleation at a given site. These equiaxed grains are typically limited to the melt pool surface during AM where favorable conditions for equiaxed grain nucleation, *i.e.*, low G and high solidification rate(V) are present.

The criteria for a transition from columnar to equiaxed (CET) microstructure are given by Hunt's model as follows:

$$G < 0.617 N_o^{\frac{1}{3}} \left(1 - \frac{(\Delta T_n)^3}{(\Delta T_c)^3}\right) \Delta T_c \qquad [1]$$

Equation [1] indicates that for a given G, increasing the nucleant particle density (N_o), increasing the potency of particles (at low ΔT_n), and maximizing the degree of ΔT_c the nucleation of equiaxed grains can be enhanced and in turn promote a CET.[9,11,12] The above criteria suggest that control of solidification parameters can be used to promote the nucleation of equiaxed grains and reduce anisotropy. This can be achieved by manipulating the process parameters (scan strategy, scan speed, laser power, *etc.*) used during laser bed powder fusion, but the process parameter window is typically limited to avoid the formation of defects such as keyholing porosity, balling/beading, cracking, lack of fusion, *etc.*[1,13,14] Given such limitations, one other strategy to enhance the CET is through the addition of secondary "inoculant" particles that act as potent nucleating substrates. In recent years, various studies have been conducted on increasing the nucleant density by adding such inoculant particles to AM material feedstock for Al, Ti, and Ni-based alloys.[10,13,15,16]

Cobalt aluminum oxide ($CoAl_2O_4$) is one such particle that has been demonstrated to show a grain refinement effect during selective laser melting (SLM) of Inconel 718(IN718).[16] These $CoAl_2O_4$ particles have traditionally been used as inoculants for grain refinement of investment cast Ni-superalloys.[17–21] Under high temperature when in contact with liquid metal, the inoculant particles are chemically reduced by some of the reactive elements that constitute IN718 (Al, Ti, Cr) to form elemental Co particles:

$$\begin{aligned} CoAl_2O_4 + \frac{2}{3}Cr &\rightarrow \frac{1}{3}Cr_2O_3 + Co + Al_2O_3 \\ CoAl_2O_4 + \frac{2}{3}Al &\rightarrow \frac{4}{3}Al_2O_3 + Co \\ CoAl_2O_4 + \frac{1}{2}Ti &\rightarrow \frac{1}{3}TiO_2 + Co + Al_2O_3 \end{aligned} \qquad [2]$$

Crystallographic matching at the inoculant–matrix interface has typically served as a good indicator for the potency of nucleating substrates in terms of the low ΔT_n required to nucleate grains, and the formation of solid Co particles is ideal as they possess an FCC lattice structure with a small lattice mismatch to the IN718 matrix.[22–25] Prior work on AM of IN718 + $CoAl_2O_4$ has focused on assessing the effect of minor additions (0.2 wt pct),[16] but an increase in $CoAl_2O_4$ content has been reported to lead to an increased grain refinement effect for investment castings.[21] However, for the extreme thermal conditions and multiple remelting/solidification cycles that are associated with AM processes such as SLM, the behavior of these inoculant particles is not well understood. For this reason, this investigation is aimed at studying the influence of nucleant density on the grain refinement during SLM IN718 by varying the weight fraction of $CoAl_2O_4$ inoculant particles from 0 to 2 wt pct.

II. EXPERIMENTAL PROCEDURE

For this study, gas-atomized IN718 powder supplied by Chia Yi Steel Inc., and $CoAl_2O_4$ inoculant supplied by Alfa Aesar Inc were used. The nominal composition of the IN718 powder is given in Table I, and the particle size distribution (PSD) [D_{10}:D_{50}: D_{90}] for the two powders is given as IN718 [19:32:55 μm] and $CoAl_2O_4$[0.3:2.6:6.1 μm]. Powder mixtures of 0.2, 1.0, and 2.0 wt pct $CoAl_2O_4$ powders with IN718 powder were prepared by ball milling with a roller mill set to a speed of 130 rpm for 1 hour. An inhouse SLM machine at the National Tsing Hua University was used to produce 10 mm size cubes with 0, 0.2, 1.0, and 2.0 wt pct addition of $CoAl_2O_4$ on a carbon steel baseplate with a laser parameter set optimized for building specimens with a density of ≥ 99.5 pct. This parameter set included a laser power of 220 W, a hatch speed of 800 mm/s ,a hatch distance of 100 μm, and a zig-zag scan strategy with 67 deg rotation (67-rot) of scan direction between subsequent layers. In addition to the 67-rot scan strategy specimens, a second set of 0 and 0.2 wt pct specimens was also produced using a single direction scan strategy and 800 mm/s hatch speed. The 10 mm cubes were detached from the baseplate by wire electro-discharge machining (EDM). Specimens were sectioned in half and one half underwent a supersolvus solution heat treatment (SHT) at 1100 °C for 2 hours, followed by air cooling.

Following standard metallographic preparation procedures of the specimens, characterization of the oxide distribution and melt pool size was conducted using a Nikon metallograph. A Kalling's No.2 etchant (5 g $CuCl_2$ + 100 ml HCL + 100 mL ethanol) was used to reveal the melt pool morphology. After SLM, the inoculant particle size distributions were quantified using ImageJ software with an equivalent particle diameter of 10 μm used as the minimum particle size cutoff during image processing and analysis. For further microstructural characterization, a JEOL JSM-6701F field emission scanning electron microscope (FESEM) equipped with a Bruker EDS detector was used with an accelerating voltage of 5 and 15 kV under secondary electron mode (SE). Electrolytic etching with a 10 pct H_3PO_4 solution in H_2O was used to reveal the cellular microstructure.

Grain morphology, grain size distribution, and grain misorientation were characterized using an Oxford Instruments Nordlys Nano electron backscatter diffraction (EBSD) detector attached to a JEOL JSM 5900-LV scanning electron microscope (SEM). EBSD scans were obtained at low (× 100) and high (× 250)

Table I. Nominal Composition of IN718 Powder

	Ni	Co	Cr	Fe	Al	Cu	Ti	Si	Mn	Mo	Nb	C
Wt Pct	bal.	0.1	18.3	16.8	0.6	0.04	1	0.1	0.1	3	5.2	0.06

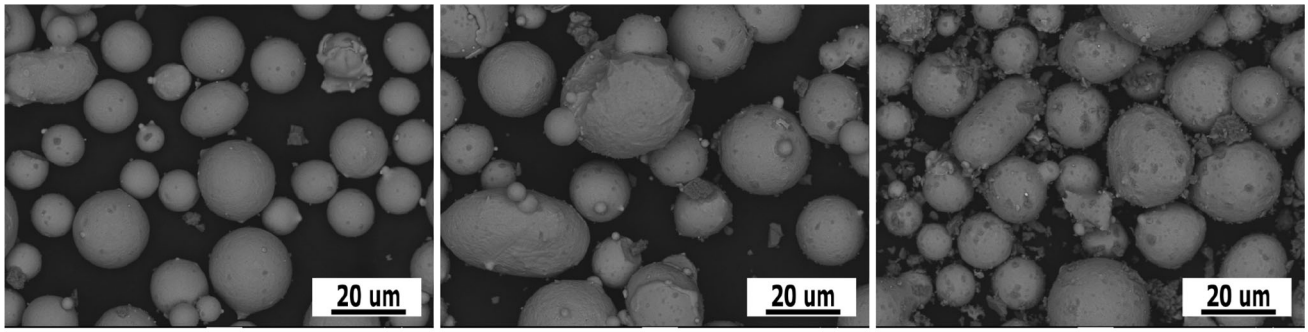

Fig. 1—SEM images showing the morphology of IN718 powder mixed with (*a*) 0.2 wt pct, (*b*) 1 wt pct, and (*c*) 2 wt pct $CoAl_2O_4$ powder.

magnifications (Mag) with a step size of 2.5 and 0.5 μm. For a representative measurement of the aspect ratio (AR)/grain size distributions, a minimum of 3 low magnification scans were obtained from a 1 mm^2 area with a 10 μm minimum grain size threshold. Samples were characterized in the vertical (*XZ*) plane along the center of the cuboid and the (transverse) *XY* plane at *Z* ~ 5 mm from the baseplate. The grain size, AR, and intragranular misorientation distributions were obtained using EBSD channel 5-HKL software with a minimum misorientation of 10 deg for grain boundaries and inclusion of border grains without weighting.

III. RESULTS

A. *As-Built (AB) Microstructure*

The morphology of IN718 powders mixed with increasing weight fraction of $CoAl_2O_4$ is shown in Figure 1. From the scanning electron micrographs, it can be observed that ball milling the IN718 powder with + 0.2 wt pct $CoAl_2O_4$, Figure 1(a), leads to a powder morphology where fine 1 to 3 μm size inoculant particles are mechanically attached as satellites to the powder surface. As the $CoAl_2O_4$ weight fraction increases to 1 and 2 wt pct, Figures 1(b) and (c), larger inoculant particles with sizes on the order of approximately 3 to 10 μm were found embedded into the powder surface. In addition to these satellite particles, agglomerated inoculants that were > 10 μm were observed to lie adjacent to the IN718 powder. The frequency of these larger non-satellite particles appears to be proportional to the weight fraction of inoculant. Also, the approximate size of inoculant particles observed in the powder mixtures shows good agreement with the PSD of the $CoAl_2O_4$ ($[D_{10}{:}D_{50}{:}D_{90}]$ = [0.3:2.6:6.1 μm].

Following SLM processing, the microstructure of the IN718 + $CoAl_2O_4$ samples was observed to contain a number of large non-metallic slag particles with sizes ranging from 10 to 100 μm. These non-metallic inclusions are much larger than the $CoAl_2O_4$ inoculant particles observed in the powder mixture and outside of the initial PSD, suggesting severe agglomeration during the SLM process. Figure 2 shows the morphology and spatial distribution of these agglomerates after SLM. Results from quantitative digital image analysis, in Table II, reveal that the particle density, average particle size, and volume fraction of agglomerates increase with inoculant weight fraction. The volume fraction of agglomerates reported in Table II also shows good agreement with the added volume fraction of inoculant, which happens to be within 1 to 2 standard deviations of the measured values. From the particle density distribution in Figure 2(d), it can be noted that there is a sharp drop in the particle density with increasing equivalent particle diameter for samples containing + 0.2 wt pct in comparison to + 1 and + 2 wt pct $CoAl_2O_4$. The particle size characteristics after SLM show that a high-volume fraction of inoculant relative to the added amount becomes agglomerated, with the average size and frequency of agglomerates being proportional to the inoculant weight fraction.

Further characterization of the inoculant particles after SLM was done using FESEM and EDS, shown in Figure 3. Figure 3(a) displays the change of the cellular/dendritic substructure and orientation directly adjacent to the agglomerated inoculant particles. Regions possessing distinct cellular morphology were found adjacent to agglomerates, which likely correspond to fine grains formed due to the interference of melt pool solidification conditions by these agglomerates. Despite the agglomeration features observed in Figure 2, a fine dispersion of submicron oxide particles was also observed within the microstructure of the SLM

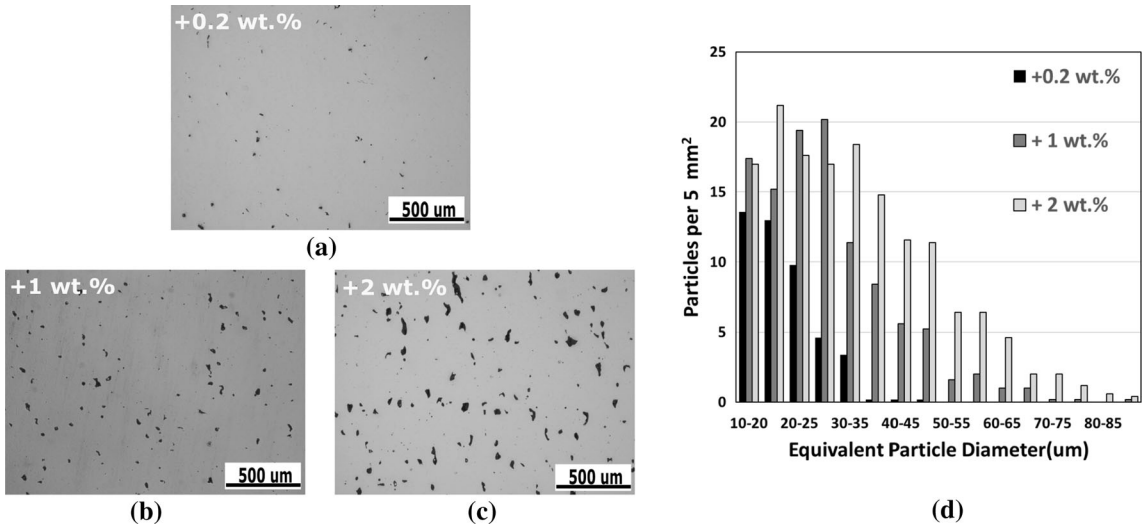

Fig. 2—Optical images showing morphology and distribution of agglomerates in the IN718 matrix after SLM with (*a*) 0.2 wt pct, (*b*) 1.0 wt pct, and (*c*) 2.0 wt pct $CoAl_2O_4$ addition. The corresponding (*d*) particle density distributions for optical images (a to c).

Table II. Particle Size Characteristics for $CoAl_2O_4$ Agglomerates After SLM

Wt Pct	0.2	1	2
Particle Density (Particles Per 5 mm^2)	45 ± 4.5	109 ± 12	153 ± 8
Average Particle Diameter (μm)	21 ± 7	31 ± 10	38 ± 12
Area Fraction (Pct)	0.3 ± 0.01	1.6 ± 0.2	3.4 ± 0.2
Added Volume Fraction (Pct)	0.37	1.83	3.62

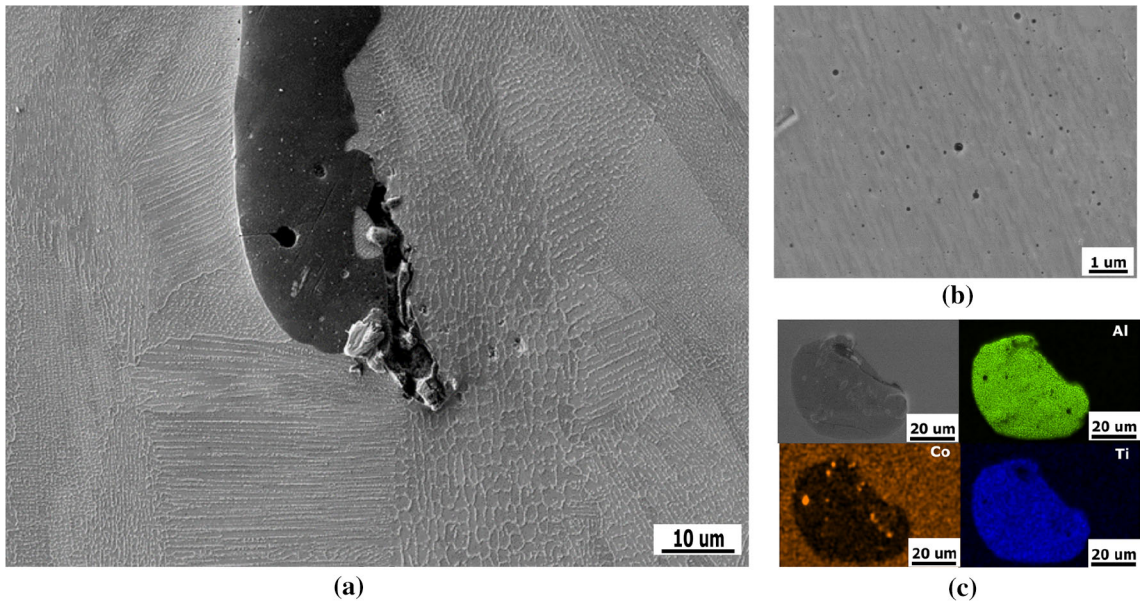

Fig. 3—(*a*) FESEM image of agglomerated oxide particle in the XZ plane of the IN718 + $CoAl_2O_4$ matrix. (*b*) A fine uniform dispersion of nano-oxides present within IN718 + $CoAl_2O_4$ matrix. (*c*) EDS compositional maps of an agglomerated oxide particle found within IN718 + $CoAl_2O_4$ matrix (Color figure online).

IN718 + $CoAl_2O_4$ samples. EDS compositional maps of the agglomerated inoculant in Figure 3(c) reveal the presence of metallic Co-rich particles contained within the oxide slag. EDS point analysis results given in Table III give a more clearly painted picture showing that the $CoAl_2O_4$ is now primarily Al_2O_3 and that the

metallic Co-rich particles contain significant concentrations of Ni and Cr.

Figure 4 shows the melt pool morphology for the optimized parameter set with the 67-rot scan strategy. The average melt pool separation distance was measured to be ~ 94 μm, and in the topmost layer, the melt pool depth was measured to be ~ 181 μm. This indicates that for the chosen layer thickness of 50 μm, that upon melting of a newly deposited layer, the previously deposited 3 to 4 layers are re-melted and that there exists an ~ 52 pct overlap in terms of maximum depth between melt pools for specimens produced with the optimized parameter set. It can also be noted that the spatial distribution of agglomerated oxide particles appears to be relatively random in the vertical (*XZ*) plane, Figure 4(a). A more noticeable pattern in the distribution of agglomerated oxide is found in the transverse (*XY*) planes and in the topmost layer, Figures 4(b) and (c), where agglomerated inoculant is located at the hatch boundaries and trailing edges of the melt pool.

The influence of the $CoAl_2O_4$ on the grain structure of the SLM IN718 was characterized using EBSD. High magnification EBSD inverse pole figure (IPF) Z maps of the grain structure of the AB IN718 + $CoAl_2O_4$ in the *XZ* plane are shown in Figure 5(a). The IPF Z maps show that the grain structure has been modified, but in a counterintuitive manner, it becomes more elongated/columnar than equiaxed. Although a modest difference in grain structure can be observed with inoculant addition, the grain size distributions presented in Figure 5(b) do not reflect this change. However, the grain aspect ratio (AR) distributions, Figure 5(c), reflect the difference in grain structure with a higher frequency of grains with AR > 2 for inoculated IN718.

Table III. Composition of Reduced Oxide and Cobalt-Rich Particles

(Wt Pct)	Ni	Co	Cr	Al	Ti	O
Oxide	0.1	0.0	8.07	32.1	10.8	44.9
Co-Rich Particle	27.3	33.0	15.5	3.5	1.1	3.4

In addition to the low magnification scans, several higher-resolution EBSD IPF Z maps were obtained over small areas for AB IN718 + $CoAl_2O_4$ for both *XY* and *XZ* planes in Figure 5(a). In the *XZ* plane with + 0 wt pct $CoAl_2O_4$, the grain structure consisted of large blocky columnar grains with fine equiaxed grains dispersed throughout. The addition of $CoAl_2O_4$ resulted in these blocky grains becoming increasingly obfuscated by thin columnar grains (most noticeably with + 1 and + 2 wt pct $CoAl_2O_4$). Similarly, the grain structure in the *XY* plane for samples with + 0 wt pct $CoAl_2O_4$ consists of blocky grains extending across the hatch width, alongside fine-grained regions at the hatch boundaries. The addition of inoculant particles eliminates the blocky grain structure along these regions as well and appears to create randomly distributed areas of fine grains within the hatch. The refined equiaxed grain structure observed in the *XY* plane with inoculant addition corresponds to the cross section of the thin columnar grains present in the XZ plane. One additional observation was that the fine grains ~ 2 to 5 μm in size adjacent to agglomerated inoculant particles in both *XY* and *XZ* planes likely correspond to the regions possessing the distinct cellular substructure shown in Figure 3(a).

To further establish the effect of $CoAl_2O_4$ on microstructure modification of SLM IN718, pole figures corresponding to the vertical (*XZ*) plane from 67-rot scan strategy SLM IN718 + 0 wt pct and + 0.2 wt pct $CoAl_2O_4$ were obtained and presented in

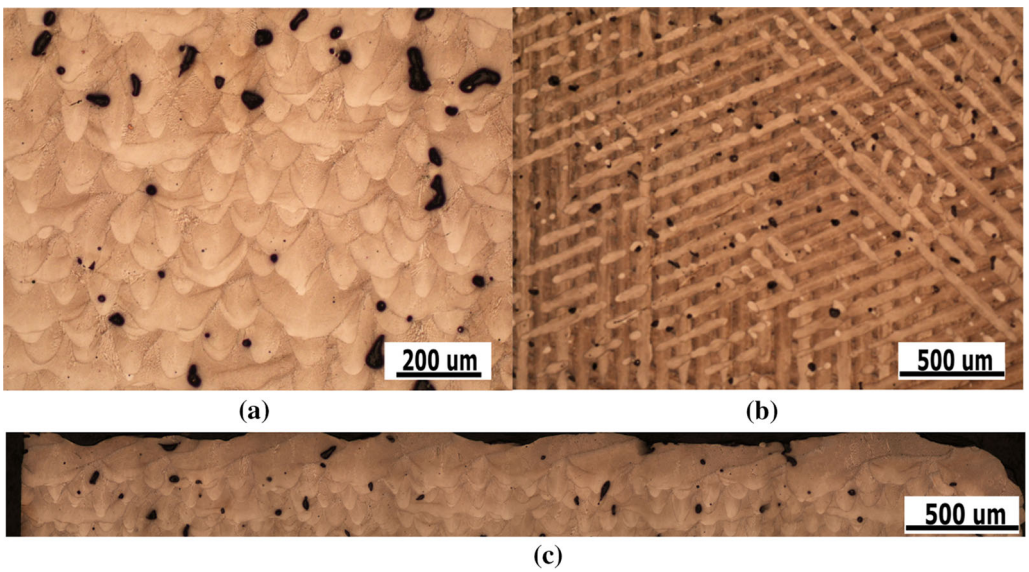

Fig. 4—Melt pool morphology of IN718 + 1.0 wt pct $CoAl_2O_4$ in the (*a*) *XZ* plane, (*b*) *XY* plane, and (*c*) melt pool and oxide morphology within the topmost layers.

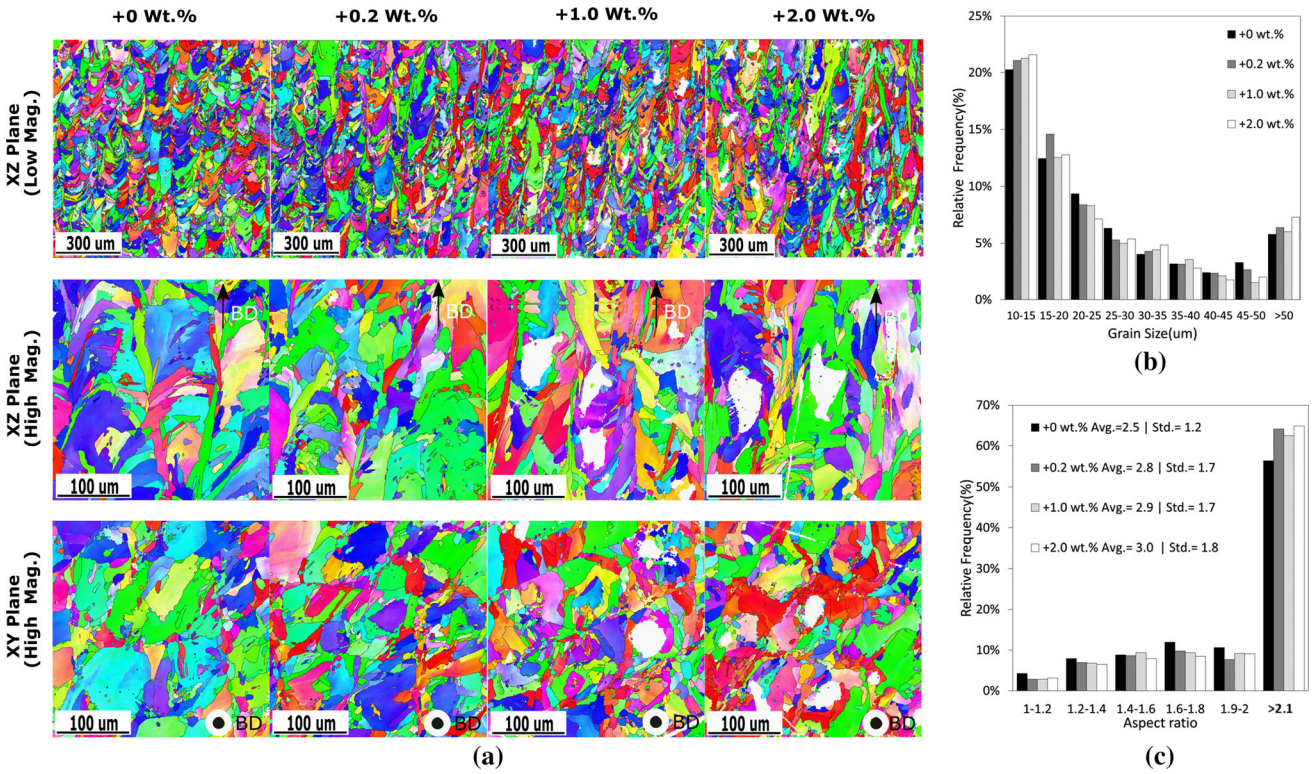

Fig. 5—(*a*) EBSD IPF Z maps of AB SLM IN718 + 0, 0.2, 1.0, and 2.0 wt pct $CoAl_2O_4$ under low magnification in the *XZ* plane and high magnification in the *XZ* and *XY* planes, with corresponding (*b*) grain size and (*c*) aspect ratio distributions from the low magnification scans. (Regions shaded in white are unindexed regions corresponding to the agglomerated inoculant).

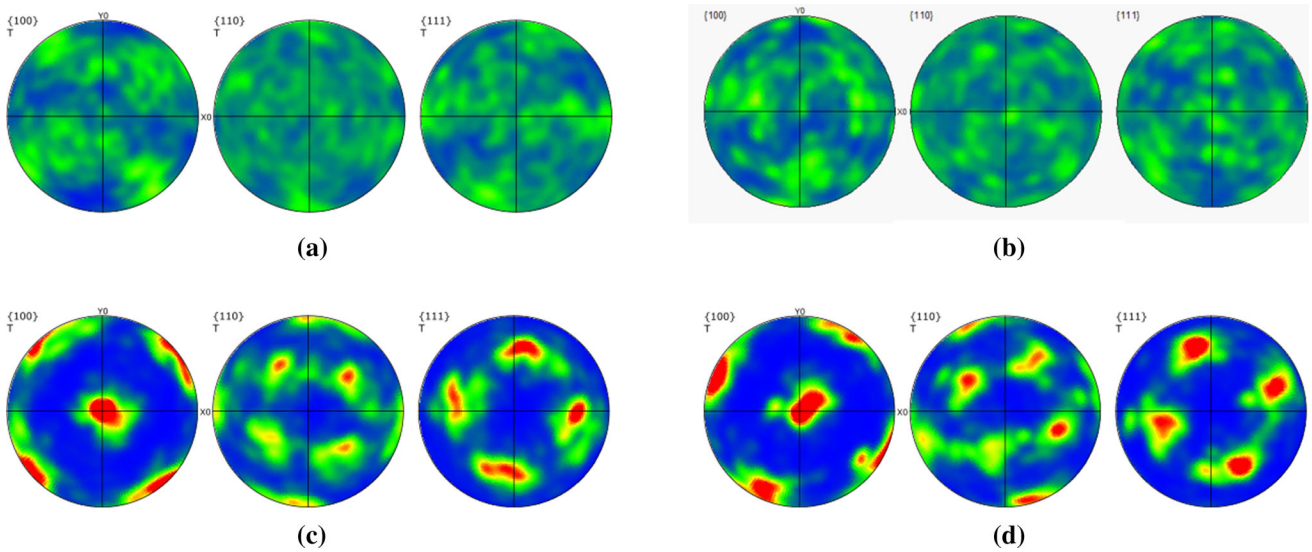

Fig. 6—EBSD pole figures corresponding to the vertical (*XZ*) plane for 67-rot scan strategy IN718 (*a*) + 0 wt pct and (*b*) + 0.2 wt pct $CoAl_2O_4$; alongside pole figures for single direction scan strategy (*c*) + 0 wt pct and (*d*) + 0.2 wt pct $CoAl_2O_4$ in the *XZ* plane.

Figures 6(a) and (b), revealing that the texture of IN 718 with $CoAl_2O_4$ remains relatively random. Given the random texture inherent to the 67-rot scan strategy, a comparison of texture for specimens fabricated with a single direction scan strategy, Figures 6(c) and (d), was made to clarify the effect on inoculant on texture. The pole figures for the single direction scan strategy specimens display a strong ⟨100⟩ and ⟨101⟩ texture regardless of inoculant. Nominally similar differences in texture were also found for + 1 and + 2 wt pct $CoAl_2O_4$ additions. The similar difference in texture for both the 67-rot and single direction scan strategy specimens suggests that the $CoAl_2O_4$ additions did not significantly affect the texture in the AB microstructure.

B. *Effect of Inoculant on Solution Heat Treatment*

To evaluate the effect of $CoAl_2O_4$ on the grain recrystallization and grain growth behavior during SHT, EBSD was used to reveal the degree of intergranular misorientation present for IN718 + $CoAl_2O_4$ before and after a supersolvus SHT at 1100 °C for 2 hrs., Figure 7. The intergranular misorientation maps for the AB IN718 + 0.2 and + 2 wt pct, Figures 7(a) and (b), show that subgrain boundaries, highlighted by green intensity regions, are present with similar frequency for both low and high inoculant content. For the + 2 wt pct addition, a higher degree of intergranular misorientation was found along the interface between the agglomerated inoculant and surrounding IN718, possibly corresponding to residual stress generated by thermal expansion mismatch between the two materials. The intragranular misorientation distributions, Figure 7(e), support that misorientation remains roughly the same irrespective of inoculant content. A slight increase in the relative frequency of misorientation bins greater than 0.5 deg is present for + 1 and + 2 wt pct additions but can likely be attributed to the misorientation increase near the agglomerated slag interfaces.

Following SHT, the intergranular misorientation maps for IN718 + 0.2 and + 2 wt pct, Figures 7(c) and (d), show comparable difference between one another. The magnitude of the intergranular misorientation for + 0.2 wt pct $CoAl_2O_4$ appears to decrease after SHT, Figure 7(c)., with a noticeable decrease in the number of subgrain boundaries. For + 2wt pct $CoAl_2O_4$, Figure 7(d), a large number of subgrain boundaries are still present after SHT. Similar observations were made for + 1 wt pct $CoAl_2O_4$, with the difference reflected in the intergranular misorientation distributions, Figure 7(e), which shows that similar levels of misorientation exist for + 1 and + 2 wt pct additions before and after SHT. Conversely, a noticeable increase in the frequency of misorientation bins < 0.5 deg for +0 and + 0.2 wt pct samples occurs between the AB and SHT conditions.

Low magnification IPF Z maps of the IN718 + $CoAl_2O_4$ after SHT are presented in Figures 8(a) through (d). The IN718 microstructures containing + 0 and + 0.2 wt pct $CoAl_2O_4$, Figures 8(a) and (b), were observed to have recrystallized and formed a more equiaxed grain structure when viewed in the *XZ* plane. The microstructure of IN718 containing + 1 wt pct and + 2 wt pct $CoAl_2O_4$, Figures 8(c) and (d), however, still retained the columnar grain structure present in the AB condition. Retention of the AB microstructure is accompanied by a noticeable decrease in sigma 3 ($\sum 3$) grain boundary frequency with the values being approximately 28 pct, 16 pct 1.6 pct, and 1.7 pct for + 0, + 0.2, + 1, and + 2 wt pct $CoAl_2O_4$ (the $\sum 3$ frequency was ~ 0.5 pct for the AB specimens), suggesting limited recrystallization and grain growth kinetics for IN718 + $CoAl_2O_4$. Analysis of the grain boundary characteristics for AB and SHT conditions also showed that a similar frequency of subgrains (0 to 5 deg misorientation) exists in the AB condition irrespective of inoculant, but the subgrains are consumed during SHT for + 0 and + 0.2 wt pct $CoAl_2O_4$ addition. For + 1 and 2 wt pct $CoAl_2O_4$, the same frequency of subgrains is sustained after SHT. The grain size

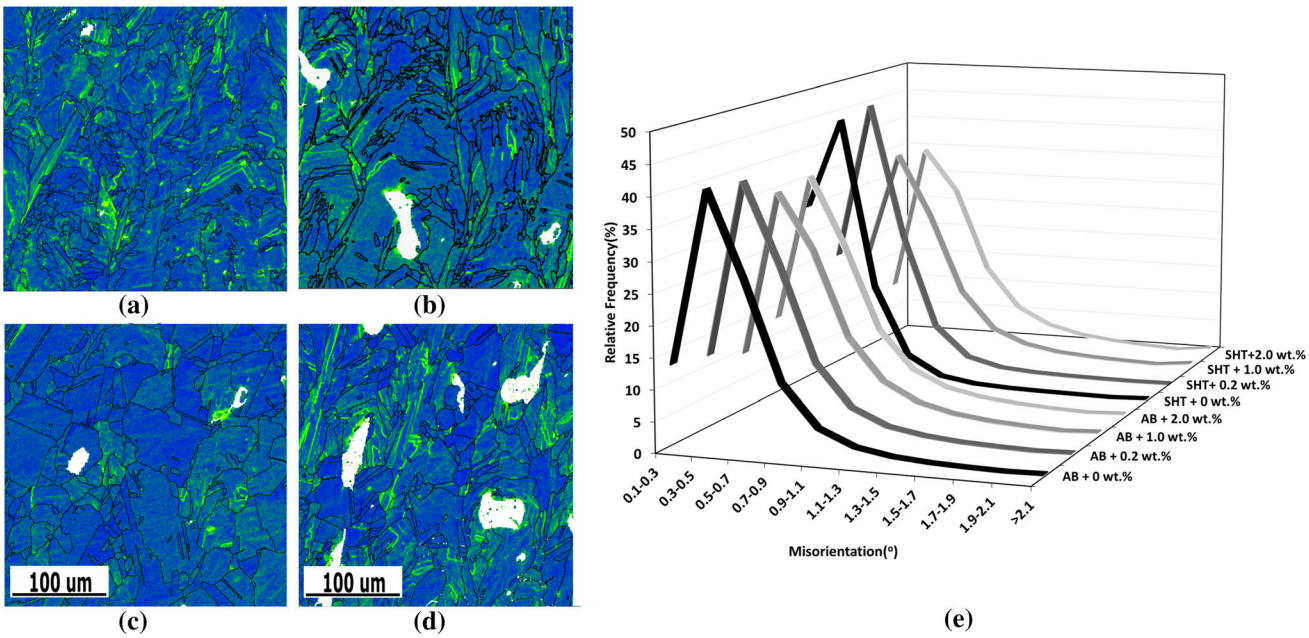

Fig. 7—EBSD intragranular misorientation maps and for (*a*) AB IN718 + 0.2 wt pct, (*b*) AB IN718 + 2 wt pct, (*c*) SHT IN718 + 0.2 wt pct, and (*d*) SHT IN718 + 2 wt pct $CoAl_2O_4$ addition. The (*e*) intragranular misorientation distributions of AB + SHT IN718 with 0, 0.2, 1.0, and 2 wt pct $CoAl_2O_4$ addition in the *XZ* plane (Color figure online).

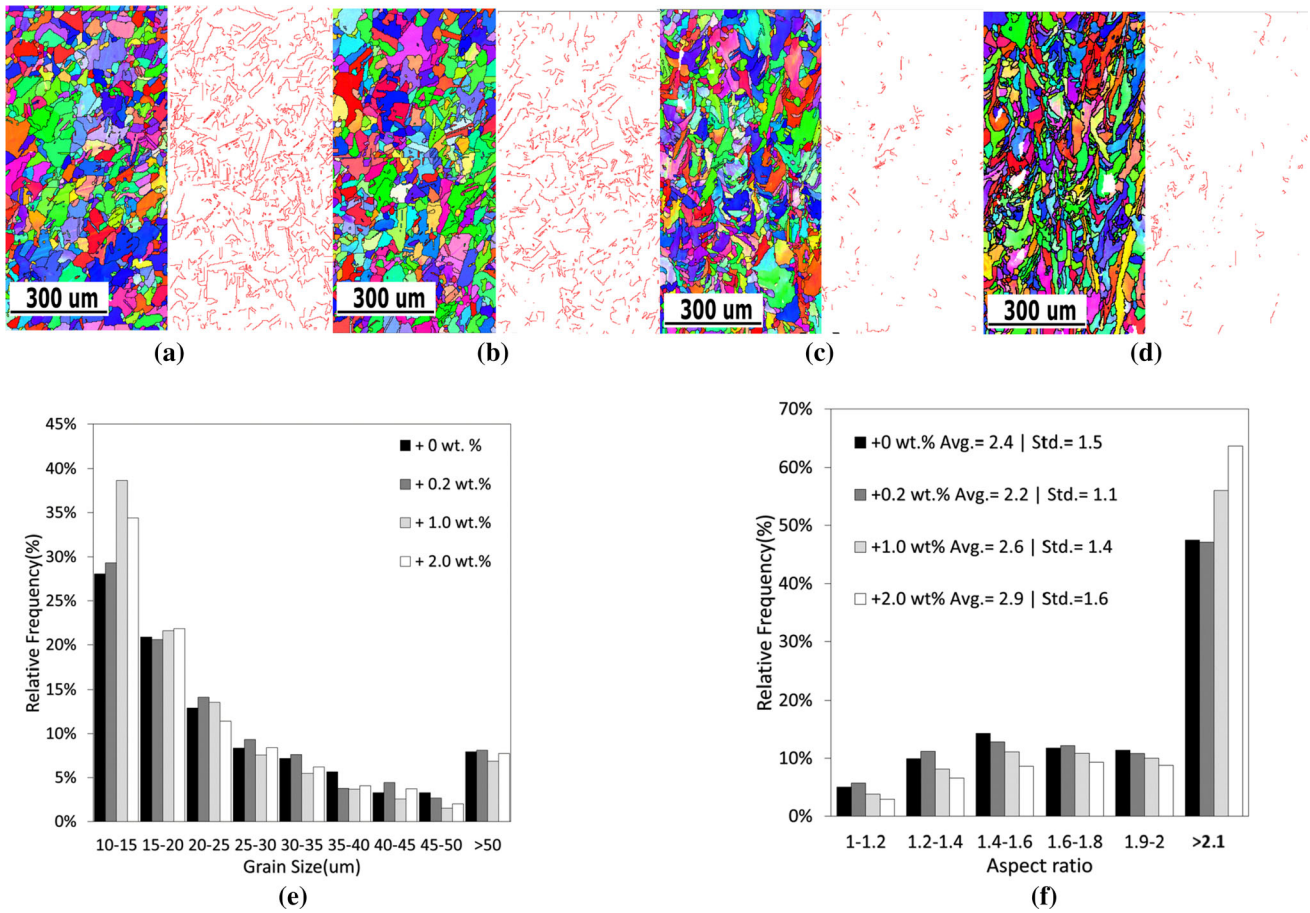

Fig. 8—(*a*) Low magnification EBSD IPF Z maps with mirror $\sum 3$ grain boundary maps of SHT SLM IN718 with (*a*) 0, (*b*) 0.2, (*c*) 1.0, and (*d*) 2.0 wt pct $CoAl_2O_4$ additions. The corresponding (*e*) grain size and (*f*) aspect ratio distributions obtained from the low magnification scans. (Regions shaded in white are unindexed regions corresponding to the agglomerated inoculant).

distributions in Figure 8(e) also show that IN718 + 1 and + 2 wt pct $CoAl_2O_4$ contain a higher relative frequency of grains within the 10 to 15 μm range that were originally present in the AB microstructure. In addition to retaining a higher fraction of fine grains, the aspect ratio distributions, Figure 8(f), show that IN718 + 1 and 2 wt pct $CoAl_2O_4$ have a higher frequency of grains with an aspect ratio > 2.

Figure 9 shows the nano-oxide particle dispersion in the SHT IN718 + $CoAl_2O_4$ samples microstructure. Qualitative image analysis and measurement of the nano-oxide volume fraction (f_v) indicate that the particle density is proportional to the inoculant weight fraction. From Figures 9(c) and (d), oxide particles are located increasingly at the grain boundaries for 1 and 2 wt pct $CoAl_2O_4$ additions suggestive of a particle pinning effect. Figure 10 shows the change in microstructure with varying concentration of $CoAl_2O_4$ added to IN718. The maps and distributions, Figures 10(a) and (b), show that a difference in area fraction of grains with aspect ratio within the range of 1 to 1.5, 1.5 to 2, and > 2 remains the same for 1 and 2 wt pct inoculant addition, while samples containing 0 and 0.2 wt pct inoculant show a decrease in area fraction of grains with aspect ratio > 2 and show an increase in area fraction of grain within the range of 1 to 1.5, and 1.5 to 2.

IV. DISCUSSION

Microstructural characterization of the as-built microstructures of SLM IN718 + $CoAl_2O_4$ revealed that there is a modest grain refinement and reduction of microstructural anisotropy when 0.2 wt pct inoculant additions are added, but increasing the concentration of the inoculant to 1 or 2 wt pct did not serve to further reduce the degree of anisotropy. The excess inoculant particles did not appear to contribute to promoting the formation of an equiaxed grain structure. The grain structure modification that has occurred presents itself as a small increase in the frequency of fine grains within the range of 2.5 to 5 μm, and a shift in grain morphology from blocky to columnar with increasing inoculant weight fraction.

The minor grain refinement and unintended grain structure modification may potentially be attributed to the SLM process conditions required to form a fully dense material. For the chosen set of processing

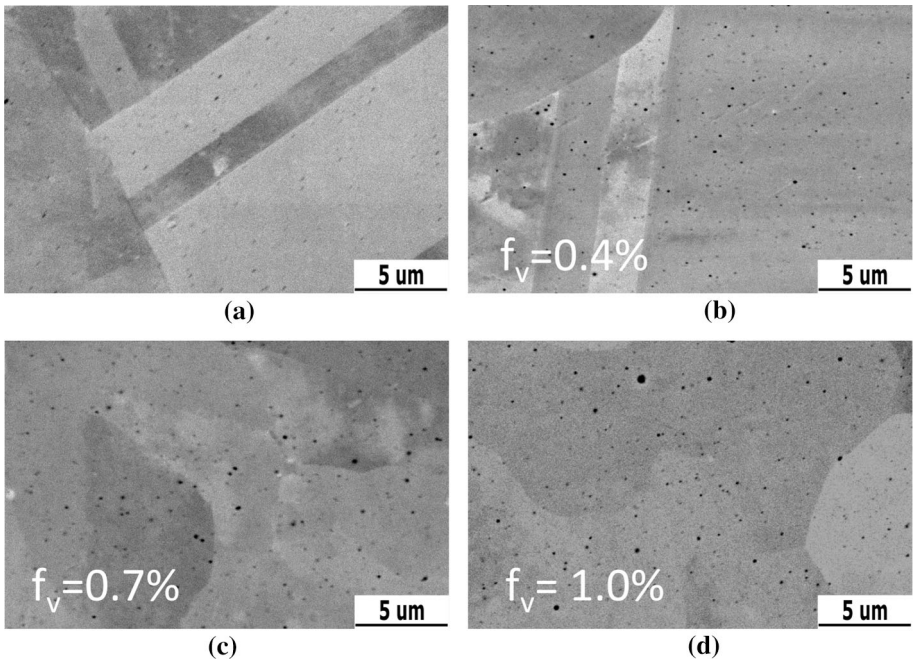

Fig. 9—Nano-oxide dispersion within SHT IN718 matrix with (*a*) 0 wt pct, (*b*) 0.2 wt pct, (*c*) 1.0 wt pct, and (*d*) 2.0 wt pct $CoAl_2O_4$ addition matrix after SHT (f_v is the volume fraction of oxide with micro/nano-porosity included).

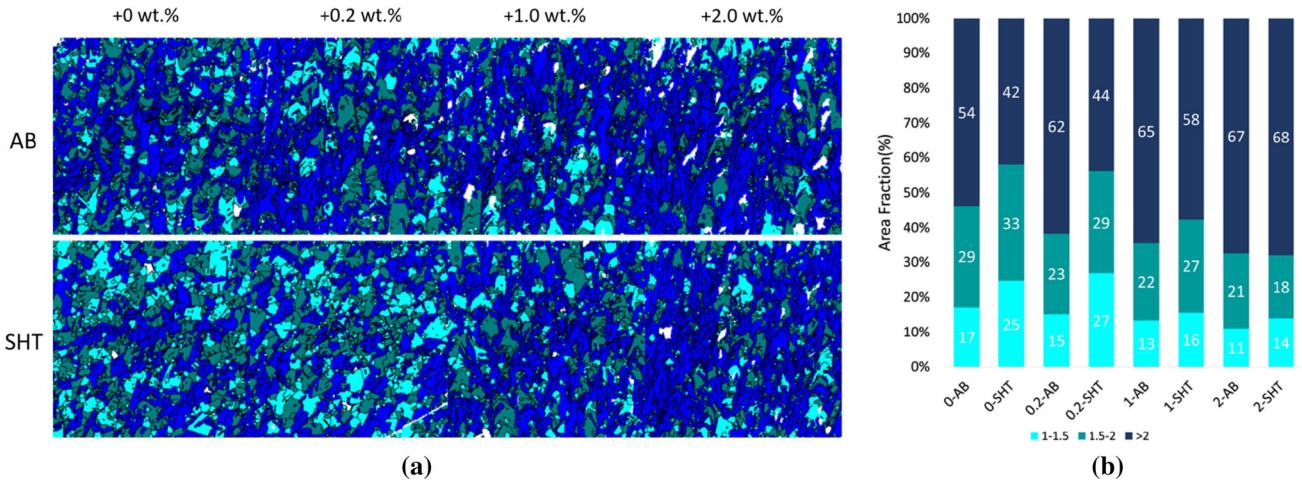

Fig. 10—Aspect ratio (AR) (*a*) maps and (*b*) AR area fraction distributions for AB/SHT SLM for IN718 + 0, 0.2, 1.0, and 2.0 wt pct $CoAl_2O_4$ in the *XZ* plane.

parameters, it was found that melt pool depth extends to a magnitude that results in remelting of and resolidification of approximately 3 to 4 previously deposited layers. As a result, the inoculant particles experience multiple melting and solidification cycles. This is further supported by the presence of large, non-metallic slag particles that are up to 100 μm diameter in size that likely agglomerated over the subsequent laser melting cycles. Although the $CoAl_2O_4$ milled together with the IN718 powder feedstock was chemically reduced to form elemental Co within the melt pool during SLM processing, it would appear that the subsequent remelting of the underlying material largely negates their ability to effectively refine the resulting grain structure.

Aside from issues associated with remelting of the deposit, the potency of inoculant particles may also be influenced by the kinetics of Co formation from the reduction of $CoAl_2O_4$ during SLM. For grain structure modification of investment castings with $CoAl_2O_4$, the degree of grain refinement is strongly dependent on the casting melt pour temperature. The lower the melt pour temperature, the stronger the grain refinement effect. In situ monitoring and computational modeling studies have consistently shown that the temperature of a laser-induced melt pool during AM can be in excess of 2000 °C.[1,26,27] The melting point of pure cobalt is 1490 °C and particles with a much higher melting temperatures such as TiC, WC_2, and La_2O_3 have been

shown to partially melt during SLM processing.[10,15,26] Giving reason to suggest that the formation of Co particles and in turn the potency of inoculants during SLM is controlled both by the rate of reduction reaction and by the rate at which Co dissolves into the liquid melt.

The free growth model by Greer, where σ is the interfacial energy between the liquid–solid interface, and S the entropy of fusion per unit volume,

$$\Delta T_n = \frac{4\sigma}{\Delta S_v d} \quad [3]$$

suggests that the nucleation potency of a particle (ΔT_n) is inversely proportional to its size (d), and that free growth and initiation of grains occur first on the largest nucleants. For a given size distribution of nucleant particles, there is a corresponding spread in the constitutional undercooling required for grain nucleation.[28–30] Due to the complexity of the melt pool physics during SLM, it is unknown whether the Co formed by reduction reaction forms discrete particles on the surface of inoculants or a uniform layer. However, with consideration of Eq. [3], this would appear to suggest that the elemental Co does not form or cannot reach an appropriate size distribution required to act as potent nucleating particles (low ΔT_n) for the amount of ΔT_c generated during the SLM process.

The by-products of the chemical reduction of $CoAl_2O_4$ are Co and Al_2O_3. Even if the Co is absorbed back into the melt pool and does not contribute to grain nucleation during solidification, the physical presence of the nano-oxides, Figure 9, in the laser-induced liquid melt pool[31,32] may be affecting the thermophysical properties. Recent studies have reported that the presence of nano-aluminum oxide particles in a laser-induced Nickel melt pool results in a slight reduction of surface tension and a considerable increase in the viscosity of the liquid.[32] For "nanofluids" in general, even a low volume fraction of nanoparticles in a host liquid can lead to a considerable increase in fluid viscosity.[33,34] An increase in the fluid viscosity may result in reduced advective heat transfer, which could translate to a lower solidification rate (V).[31] From Eq. [1], an increase in G and decrease in V favors columnar grain growth. For the case of SLM samples processed with the 1 and 2 wt pct inoculant addition, the resulting increase in fluid viscosity and decrease in V could be potentially responsible for the increased anisotropy present in the microstructure. Additionally, the presence of the nano-oxide particle dispersion in the microstructure may also contribute to modifying the microstructure and preventing grain coarsening that may occur from thermal cycling during SLM.

The challenges faced with microstructure modification of IN718 with $CoAl_2O_4$ can be summarized by the interdependence theory, which suggests that the extent of equiaxed grain formation due to inoculant addition during SLM would be primarily determined by minimizing the nucleation-free zone (NFZ) between the initial epitaxial grain nucleation and subsequent nucleation events.[10,35–37] A minimal NFZ is achieved through reducing/increasing the G/V and maximizing the potency of inoculant particles (ΔT_n). These requirements closely relate to the potential problems identified for $CoAl_2O_4$ inoculant regarding process conditions, issues with Co particle formation, and nanoparticle modification of thermophysical properties. Several recent studies focused on particle migration and agglomeration for laser AM have suggested that a limited process window for which an appropriate Marangoni convection intensity and melt pool volume exist to distribute reinforcing particles uniformly.[26,27,38,39] Careful selection of process parameters would be needed to accommodate these issues, while also dealing with the particle agglomeration present for high inoculant concentrations.

The fine nano-oxide dispersions resulting from SLM of IN718 + $CoAl_2O_4$ were found to influence the recovery, recrystallization, and grain growth during post-process heat treatment. A reduction in intergranular misorientation occurred for samples containing + 0 and + 0.2 wt pct following SHT, accompanied by an increase in grain size and $\sum 3$ grain boundary frequency. However, the microstructure of SHT IN718 + 0.2 wt pct $CoAl_2O_4$ displayed a lower frequency of $\sum 3$ grain boundaries within the recrystallized specimens. The density of $\sum 3$ annealing twins is typically correlated to grain growth, suggesting a Zener particle pinning effect. The nano-oxide dispersion likely served as pinning particles that exhibited a Zener pinning pressure (P_{sz}) that counteracted the driving pressure for grain growth (P_d) following recrystallization resulting in a lower net pressure (P) acting on grain boundaries[40–43]:

$$P = P_D - P_{sz} \quad [4]$$

The magnitude of P_{sz} is typically proportional to the volume fraction (f_v) of the pinning particles, which was found to increase with inoculant content, Figure 9.

In addition to restricting growth of grains, the Zener pinning effect may also suppress the nucleation of recrystallized grains. The presence of a high density of nano-oxide particles may interfere with the annihilation and rearrangement of dislocations that occur during recovery or due to the P_{sz} can limit the growth of existing subgrains which can then act as recrystallization nuclei.[44] For the case of IN718 + 1 and + 2 wt pct $CoAl_2O_4$, some degree of interference with the recovery process and subgrain growth appears to have taken place given the marginal difference in intergranular misorientation following SHT while sustaining similar number of subgrain boundaries. Similar particle-stabilized subgrain structures have been reported for other oxide dispersion strengthened superalloys.[43] The recrystallization and grain growth that occurred for IN718 + 1 and 2 wt pct $CoAl_2O_4$ were likely at sites with increased strain energy, where the P_D was large enough to overcome the P_{sz}, leading to limited non-uniform recrystallization while maintaining the AB grain structure.

Despite the minor grain refinement effect observed, the different annealing behavior resulting from the nano-oxide dispersions formed by addition of $CoAl_2O_4$ may be promising for the employment of more aggressive post-process heat treatments for AM IN718. Optimal precipitation strengthening for AM IN718 typically requires complete dissolution of the Nb-enriched δ and Laves phases in the AB microstructure.[45] In some cases, it has been suggested that standard solution heat treatments below the δ solvus (~ 1080 °C) do not enable the complete dissolution of these unwanted phases.[46] Approaches for addressing this issue have involved using a SHT well above the solvus temperature, and/or with significantly longer hold times. Similar types of SHT have also reported to be effective for the reduction of microstructural anisotropy.[47–49] Despite the benefits, these high-temperature SHTs are accompanied by significant grain coarsening, the inability to retain the AB microstructure, and an overall reduction in stored strain energy. Provided that appropriate laser scan conditions can be identified that result in minimal agglomeration of the inoculant particles, blending the power feedstock with oxide particles may potentially enable improved microstructural control and engineering of the grain structure additively manufactured Ni-base superalloys.

V. CONCLUSION

Based on the results of this investigation, the following conclusions can be drawn:

1. Increasing the $CoAl_2O_4$ inoculant content for SLM IN718 does not translate to a more equiaxed grain structure in the as-built condition. The microstructure still shows signs of grain refinement, but at the expense of increased anisotropy and severe agglomeration of inoculant particles. This minor grain refinement and unintended grain structure modification may be due to several process-related issues: remelting of inoculant, thermal conditions leading to unfavorable Co particle formation kinetics, and modification of thermophysical conditions in the presence of nano-oxide particles.
2. Further optimization of process parameters will be required to generate the solidification conditions favorable for equiaxed grain formation by $CoAl_2O_4$. Favorable solidification conditions include a small nucleation-free zone for the epitaxial grains present at the onset of solidification and limited remelting of inoculant particles + underlying material. Simultaneously, the process window space would be required to minimize particle agglomeration and other process-induced defects.
3. Despite severe particle agglomeration, a fine dispersion of nano-oxide particles that hinder grain growth and recrystallization during post-heat treatment are found in the as-built microstructure. The density of nano-oxide particles appears to be proportional to inoculant content, resulting in limited recrystallization and retention of as-built grain structure due to a strong Zener pinning effect for IN718 specimens processed with 1 and 2 wt pct $CoAl_2O_4$ additions

ACKNOWLEDGMENTS

This work was supported by the National Science Foundation CMMI # 1663068 and the Ministry of Science and Technology (MOST), Taiwan MOST108-2218-E007-009

REFERENCES

1. T. DebRoy, H.L. Wei, J.S. Zuback, T. Mukherjee, J.W. Elmer, J.O. Milewski, A.M. Beese, A. Wilson-Heid, A. De, and W. Zhang: *Prog. Mater Sci.*, 2018, vol. 92, pp. 112–224.
2. T.M. Pollock and S. Tin: *J. Propul. Power*, 2006, vol. 22, pp. 361–74.
3. X. Wang and K. Chou: *JOM*, 2017, vol. 69, pp. 402–408.
4. M. Sadowski, L. Ladani, W. Brindley, and J. Romano: *Addit. Manuf.*, 2016, vol. 11, pp. 60–70.
5. K.N. Amato, S.M. Gaytan, L.E. Murr, E. Martinez, P.W. Shindo, J. Hernandez, S. Collins, and F. Medina: *Acta Mater.*, 2012, vol. 60, pp. 2229–39.
6. P. Tao, H. Li, B. Huang, Q. Hu, S. Gong, and Q. Xu: *Vacuum*, 2019, vol. 159, pp. 382–90.
7. S. Das: *Adv. Eng. Mater.*, 2003, vol. 5, pp. 701–11.
8. S. Kou: *Welding Metallurgy*, 2nd ed., Wiley-Interscience, Hoboken, 2003, pp. 170–87.
9. F. Yan, W. Xiong, and E. Faierson: *Materials*, 2017, vol. 10, p. 1260.
10. M.J. Bermingham, D.H. StJohn, J. Krynen, S. Tedman-Jones, and M.S. Dargusch: *Acta Mater.*, 2019, vol. 168, pp. 261–74.
11. J.A. Spittle: *Int. Mater. Rev.*, 2006, vol. 51, pp. 247–69.
12. W. Kurz, C. Bezençon, and M. Gäumann: *Sci. Technol. Adv. Mater.*, 2001, vol. 2, pp. 185–91.
13. J.H. Martin, B.D. Yahata, J.M. Hundley, J.A. Mayer, T.A. Schaedler, and T.M. Pollock: *Nature*, 2017, vol. 549, pp. 365–69.
14. P.C. Collins, D.A. Brice, P. Samimi, I. Ghamarian, and H.L. Fraser: *Annu. Rev. Mater. Res.*, 2016, vol. 46, pp. 63–91.
15. I.-T. Ho, Y.-T. Chen, A.-C. Yeh, C.-P. Chen, and K.-K. Jen: *Addit. Manufact.*, 2018, vol. 21, pp. 465–71.
16. I.-T. Ho, T.-H. Hsu, Y.-J. Chang, C.-W. Li, K.-C. Chang, S. Tin, K. Kakehi, and A.-C. Yeh: *Addit. Manufact.*, 2020, vol. 35, p. 101328.
17. F. Jian and Y. Bin: *High Temp. Alloys Gas Turbines*, 1982, vol. 1982, pp. 987–97.
18. M. Zielińska, K. Kubiak, and J. Sieniawski: *J. Achiev. Mater. Manuf. Eng.*, 2009, vol. 35, pp. 55–62.
19. F. Binczyk and J. Śleziona: *Arch. Foundry Eng.*, 2010, vol. 10, pp. 195–98.
20. F. Binczyk, J. Śleziona, and P. Gradoń: *Composites*, 2011, vol. 1, pp. 49–55.
21. F. Binczyk: *Arch. Foundry Eng.*, 2009, vol. 9, pp. 105–8.
22. B.L. Bramfitt: *Metall. Trans.*, 1970, vol. 1, pp. 1987–95.
23. D. Qiu, M.-X. Zhang, H.-M. Fu, P.M. Kelly, and J.A. Taylor: *Philos. Mag. Lett.*, 2007, vol. 87, pp. 505–14.
24. Y. Xiong, X. YingWei, J. Du, A. Yang, L. Liu, and D. Zeng: *Metall. Mater. Trans. A*, 2004, vol. 35, pp. 2111–14.
25. M. Li, J. Li, D. Qiu, Q. Zheng, G. Wang, and M.-X. Zhang: *Philos. Magn.*, 2016, vol. 96, pp. 1556–78.
26. C. Hong, D. Gu, D. Dai, A. Gasser, A. Weisheit, I. Kelbassa, M. Zhong, and R. Poprawe: *Opt. Laser Technol.*, 2013, vol. 54, pp. 98–109.
27. P. Yuan and D. Gu: *J. Phys. D*, 2015, vol. 48, p. 035303.
28. A.L. Greer, A.M. Bunn, A. Tronche, P.V. Evans, and D.J. Bristow: *Acta Mater.*, 2000, vol. 48, pp. 2823–35.

29. A.L. Greer, P.S. Cooper, M.W. Meredith, W. Schneider, P. Schumacher, J.A. Spittle, and A. Tronche: *Adv. Eng. Mater.*, 2003, vol. 5, pp. 81–91.
30. Z. Liu: *Metall. Mater. Trans. A*, 2017, vol. 48A, pp. 4755–76.
31. C. Ma, L. Chen, C. Cao, and X. Li: *Nat. Commun.*, 2017, vol. 8, pp. 1–7.
32. C. Ma, J. Zhao, C. Cao, T.C. Lin, and X. Li: *J. Manuf. Sci. Eng.*, 2016, vol. 138, p. 121002.
33. R. Prasher, D. Song, J. Wang, and P. Phelan: *Appl. Phys. Lett.*, 2006, vol. 89, p. 133108.
34. I.M. Mahbubul, R. Saidur, and M.A. Amalina: *Int. J. Heat Mass Transf.*, 2012, vol. 55, pp. 874–85.
35. D.H. StJohn, M. Qian, M.A. Easton, and P. Cao: *Acta Mater.*, 2011, vol. 59, pp. 4907–21.
36. D.H. StJohn, S.D. McDonald, M.J. Bermingham, S. Mereddy, A. Prasad, and M. Dargusch: *KEM*, 2018, vol. 770, pp. 155–64.
37. M. Bermingham, D. StJohn, M. Easton, L. Yuan, and M. Dargusch: *JOM*, 2020, vol. 72, pp. 1065–73.
38. D. Dai and D. Gu: *Int. J. Mach. Tools Manuf*, 2016, vol. 100, pp. 14–24.
39. P. Yuan, D. Gu, and D. Dai: *Mater. Des.*, 2015, vol. 82, pp. 46–55.
40. F.J. Humphreys and M. Hatherly: *Recrystallization and Related Annealing Phenomena*, Elsevier, Amsterdam, 2012, pp. 343–48.
41. A.O.F. Hayama, H.R.Z. Sandim, J.F.C. Lins, M.F. Hupalo, and A.F. Padilha: *Mater. Sci. Eng. A*, 2004, vol. 371, pp. 198–209.
42. H.R.Z. Sandim, A.O.F. Hayama, and D. Raabe: *Mater. Sci. Eng. A*, 2006, vol. 430, pp. 172–78.
43. Z. Oksiuta, P. Kozikowski, M. Lewandowska, M. Ohnuma, K. Suresh, and K.J. Kurzydlowski: *J. Mater. Sci.*, 2013, vol. 48, pp. 4620–25.
44. F.J. Humphreys: *Acta Mater.*, 1997, vol. 45, pp. 5031–39.
45. S. Sui, H. Tan, J. Chen, C. Zhong, Z. Li, W. Fan, and W. Huang: *Acta Mater.*, 2019, vol. 164, pp. 413–27.
46. W.M. Tucho, P. Cuvillier, A. Sjolyst-Kverneland, and V. Hansen: *Mater. Sci. Eng. A*, 2017, vol. 689, pp. 220–32.
47. N. Kouraytem, J. Varga, B. Amin-Ahmadi, H. Mirmohammad, R.A. Chanut, A.D. Spear, and O.T. Kingstedt: *Mater. Des.*, 2021, vol. 198, p. 109228.
48. W.M. Tucho and V. Hansen: *J. Mater. Sci.*, 2019, vol. 54, pp. 823–39.
49. E. Chlebus, K. Gruber, B. Kuźnicka, J. Kurzac, and T. Kurzynowski: *Mater. Sci. Eng. A*, 2015, vol. 639, pp. 647–55.